arXiv:2305.08710v1 [astro-ph.IM] 15 May 2023

EASpy: Fast simulation of fluorescence and Cherenkov light from extended air showers at large zenith angles

Ali Baktash [1] **and Dieter Horns**

University of Hamburg,
Faculty of Mathematics, Informatics and Natural Sciences,
Institut fuer Experimentalphysik,
Luruper Chaussee 149, 22761 Hamburg

E-mail: ali.baktash@uni-hamburg.de

ABSTRACT: The detailed simulation of extended air showers (EAS) and their emission of Cherenkov and fluorescence light requires increasing computation time and storage volume with increasing energy of the primary particle. Given these limitations, it is currently challenging to optimize configurations of imaging air Cherenkov telescopes at photon energies beyond approximately 100 TeV. Additionally, the existing simulation frameworks are not capable of capturing the interplay of Cherenkov and fluorescence light emission at large zenith angle distances ($\gtrsim 70°$), where the collection area of Cherenkov telescopes considerably increases. Here, we present EASpy, a framework for the simulation of EAS at large zenith angles using parametrizations for electron-positron distributions. Our proposed approach for the emission of fluorescence and Cherenkov light and the subsequent imaging of these components by Imaging Atmospheric Cherenkov Telescopes (IACTs) aims to provide flexibility and accuracy while at the same time it reduces the computation time considerably compared to full Monte Carlo simulations. We find excellent agreement of the resulting Cherenkov images when comparing results obtained from EASpy with the de-facto standard simulation tool CORSIKA and sim_telarray. In the process of verifying our approach, we have found that air shower images appear wider and longer with increasing impact distance at large zenith angles, an effect that has previously not been noted. We also investigate the distribution of light on the ground for fluorescence and Cherenkov emission and highlight their key differences to distributions at moderate zenith angles.

---

[1]Corresponding author.

Contents

1 Introduction

Extended air showers (EAS) provide a unique opportunity to study cosmic rays with ground based observations. At increasing energy, the sensitivity of particle detectors, e.g. Imaging Atmospheric Cherenkov Telescopes (IACTs), to observe the produced Cherenkov and fluorescence light from an EAS depends primarily on the collection area $A_{\rm eff}$. As a consequence of the limited collection area of the current generation of IACTS, the gamma-ray sky at energies above 100 TeV remains largely unexplored. The photon rate from the Crab Nebula, one of the brightest steady Galactic gamma-ray sources, for a collection area of $A_{\rm eff} = 1\,{\rm km}^2$ is less than one photon per 100 h [1]. One way to increase $A_{\rm eff}$ is to use multiple IACTs (~ 100) commonly placed with a distance of the order of ~ 100 m apart from each other [2]. A more budget-friendly approach is to make use of fewer stand-alone telescopes observing at large zenith angles (LZA), which typically means zenith

angles larger than 70°. With observations at LZA the distance to the shower is greatly increased (50 km to 100 km) which consequently expands the light pool on the ground [3] (albeit at the cost of increased attenuation due to a larger photon path to the observer). The MAGIC collaboration has already successfully demonstrated that observations at a zenith angle range of 70° to 80° increase the collection area to be larger than a square km. With an observation time of ∼ 56 h, they were able to detect γ-ray emission from the Crab Nebula up to energies of 100 TeV [4].

So far, the operational and planned IACT arrays have been optimized for observations at small zenith angles. The optimization of their configuration at large zenith angles requires a substantial effort in simulating a large number of air showers at high energies and their detection with a variety of telescope layouts, camera sizes, mirror diameters, etc. In the context of performance studies, Monte Carlo simulations, e.g. CORSIKA (see Appendix A.1), have become essential in order to optimize IACTs and reconstruction methods. Although CORSIKA is not able to simulate fluorescence light, there has been work done by the community to implement fluorescence emission in CORSIKA ([5], [6]). A general downside of these Monte Carlo simulations is the increased computation time with higher primary particle energies (and to an lesser extend increased storage size).

A simplified approach to make simulations more time-efficient is to use parametrizations which describe the distribution of charged particles in an EAS rather than simulating the shower development and keeping track of each particle generated. Commonly used analytical functions for the longitudinal number of charged particles in an EAS are the Greisen [7] or Gaisser-Hillas [8] function and for the lateral distribution the Nishimura-Kamata-Greisen function [9]. The former mentioned functions together with parametrizations of fluorescence and Cherenkov light emission [10] have been used in ShowerModel [1] to simulate the light emission in EAS and its detection by IACTs. While parametrizations tend to miss the fluctuations in the shower development, this is less of a problem at higher primary particle energies. Here, the fluctuations are considerably smaller than at lower energies.

In this work we present EASpy, a 3.5-dimensional simulation of EAS based on parametrizations for electron-positron distributions and its consequent emission of fluorescence and Cherenkov light in a analytical way while taking into account the curvature of Earth's atmosphere. As in ShowerModel, our simulation aims to compute the detector response in a fast pace but at the same time reach a high level of accuracy and flexibility. Here, we focus on photon-initiated showers to establish the method and compare the results obtained using EASpy with CORSIKA and sim_telarray, independent of particular hadronic interaction models.

One of the reasons why ShowerModel is not applicable for LZA observations is that it does not take into account the curvature of Earth's atmosphere, which can not be neglected anymore for the zenith angle range discussed in this work. In Table 1, we provide an overview of some properties for CORSIKA/sim_telarray (see Appendix A.1/A.2), ShowerModel, and EASpy. Furthermore, in [5] the authors showed how for core distances lower than 8 km the detector response of one-dimensional and three-dimensional simulations is quite different in the lateral (transversal) spread of the resulting fluorescence light image. An additional motivation for this work was to not use any parametrization for Cherenkov and fluorescence light emission, since in principle the distribution of charged particles is sufficient to treat both emission types in a analytical way.

―――――――――――――――――――――――

[1]https://showermodel.readthedocs.io/en/latest/

Table 1: Comparison of properties between `CORSIKA/sim_telarray`, `ShowerModel`, `EASpy`.

	CORSIKA/sim_telarray	ShowerModel	EASpy
Simulation method	Full MC	parameterized	parameterized
Dimension (space+time)	3+1	1+1	2.5+1
Atmosphere	(sliding) plane parallel	plane parallel	spherical
Particle content	$e^\pm$, $\mu^\pm$, ν, hadrons	$e^\pm$	$e^\pm$
Fluorescence	no	yes (param.)	yes (particle based)
Cherenkov	yes (particle based)	yes (param.)	yes (particle based)
Cherenkov-light collection	ray-tracing	parametrized	geometrical approach
Zenith angle	$0° - 90°$	$0° - 70°$	$70° - 90°$
Imaging: PSF	yes	no	yes
Imaging: Pixel shape	hex./square/circ.	square	hex./square/circ.

In Section 2, we introduce the basic concepts of `EASpy` including the production of Cherenkov and fluorescence light from an EAS and the consequent collection of this light by an IACT. The simulation of the detector response is explained in Section 3 together with a comparison of shower images obtained with `EASpy` and a full air-shower simulation in Section 4. In Section 5, we finally discuss the characteristics of the Cherenkov and fluorescence photon ground distribution at LZA.

2 EASpy framework

2.1 Spherical Atmosphere

Since the fluorescence and Cherenkov light yields depend on atmospheric parameters (e.g., air density, temperature, pressure, ...) it is important to choose a suitable model for the atmosphere. Typically, at zenith angles $\leq 70°$ a plane-parallel atmosphere is assumed, i.e. that the air mass scales with the secant of the zenith angle. However, at zenith angles $\geq 70°$ the curvature of the atmosphere is not negligible anymore and a plane parallel atmosphere approximation will lead to large errors for, e.g., the slant depth and atmospheric transmission. In order to have a more precise model, the atmosphere is divided into a series of equally spaced spherical shells with a separation of 6 m. The slant distance travelled and the height of each spherical shell is calculated in a coordinate system where the origin is set to the midpoint of the Earth (see Fig. 1a).

With measurements for the air density at various heights at zenith = $0°$ one can use the spherical symmetry of the model and calculate the height dependent slant depth at LZA:

$$X(h_i, h_{i+1}) = \int_{h_i}^{h_{i+1}} \rho(h) \, ds = \overline{\rho(h_i, h_{i+1})} \, s(h_i, h_{i+1}), \qquad (2.1)$$

where $X(h_i, h_{i+1})$ is the traversed slant depth for one spherical shell with bin edges at heights h_i and h_{i+1}, $\overline{\rho(h_i, h_{i+1})}$ is the (linearly) averaged air density and $s(h_i, h_{i+1})$ is the slant distance for the
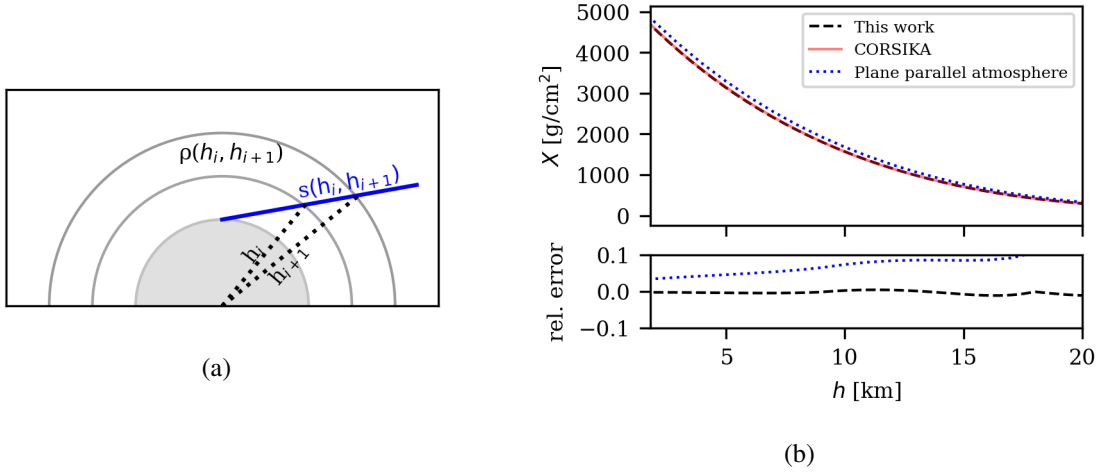
Figure 1: (a) Model of spherical atmosphere. Gray shaded area and cross denote the Earth and midpoint of the Earth, the blue line marks the path of the primary particle and the dashed lines the height of the bin edges for one spherical shell. The traversed slant distance for one spherical shell is then $s(h_i, h_{i+1})$. (b) Upper panel: Slant depth as a function of height at a zenith angle of $80°$. Lower panel: Relative error for plane parallel atmosphere and this work compared to CORSIKA.

primary particle path between the bin edges[2]. In Fig. 1b, a comparison between CORSIKA (compiled with the "CURVED" option), plane parallel atmosphere and this work is shown for the height dependent slant depth at a zenith angle of $80°$. One can observe that the results from CORSIKA and this work are in good agreement while for a plane parallel atmosphere model the relative error compared to the CORSIKA results is $\simeq 5\%$ at observation level and increasing with height.

2.2 Atmospheric transmission

The atmospheric transmission for Cherenkov and fluorescence light generated by air showers at large zenith angles is smaller than at small zenith angles. Since the position of the shower maximum is observed at a distance of $50\,\text{km}$ to $100\,\text{km}$, more light will be scattered and absorbed in the atmosphere. The resulting transmission has been calculated using the MODTRAN [11] program which takes into account Rayleigh- and Mie-scattering as well as absorption processes with a moderate spectral resolution. The program offers a wide choice of pre-defined atmospheric conditions. We use the tropical atmosphere with a desert-type haze (aerosol) condition.

In a plane parallel atmosphere model one would calculate the transmission T for a vertical path and assume that $\tau \propto \sec(\theta)$, where τ is the optical depth with $T = \exp(-\tau)$. In comparison to a spherical atmosphere, this approach would overestimate the mass overburden resulting in an underestimate of the transmission. In Fig. 2, one can observe that a plane parallel atmosphere model would underestimate the transmission by $\sim 10\%$ and that the transmission for a wavelength of $\sim 500\,\text{nm}$ is reduced by a factor of 2 for a path with $80°$ zenith angle compared to a vertical path.

---

[2]with $\rho \propto \exp(-h/h_0)$ and $h_0 \gg \Delta h$, the linear approximation for ρ in a shell is sufficiently accurate
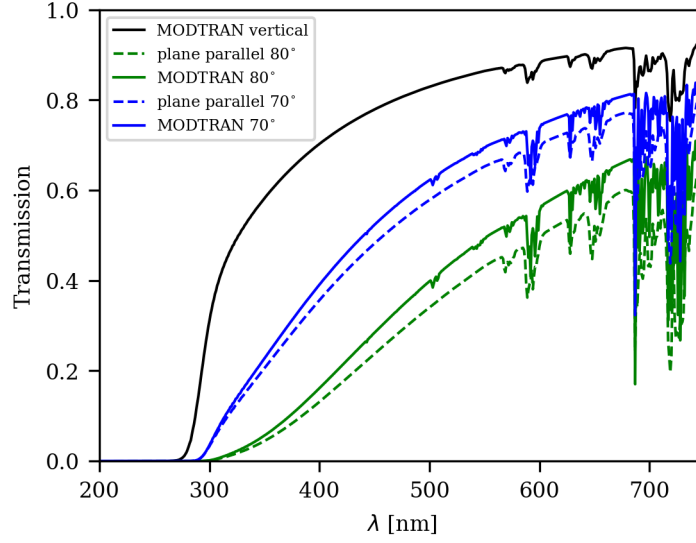
Figure 2: Transmission from 15 km to 1.8 km height for a range of wavelengths λ for a vertical path, 70° and 80° zenith angle. Transmission profiles calculated with `MODTRAN` are for tropical atmospheric profile and desert haze.

Furthermore, as expected, the difference between a plane parallel atmosphere approximation and the `MODTRAN` results is lower for a path with 70° zenith angle compared to 80° zenith angle.

The simulation tool provides a choice between using the plane-parallel approximation or to provide a set of tables of the transmission for different values of zenith angle.

2.3 Parametrizing the electromagnetic shower component

In order to simulate fluorescence and Cherenkov light from air showers one needs to accurately describe the distribution of charged particles, and most importantly the distribution of electrons and positrons since these particles are the most abundant charged particles in air showers. In this work we use a multi-dimensional parametrization for the electron-positron distributions for particle energy, angular spectrum and lateral distance proposed by [12].

The Ansatz for the parametrization of the differential particle number n in a logarithmic interval $[\ln \epsilon, \ln \epsilon + \mathrm{d} \ln \epsilon]$ of kinetic energy ϵ of electrons and positrons in MeV follow from Eqn. 6 in Ref. [12]

$$\mathrm{d}N = n(t) \, \mathrm{d} \ln \epsilon, \tag{2.2}$$

for the particle number n_Ω in a differential interval of solid angle $[\Omega, \Omega + \mathrm{d}\Omega]$ given in Eqn. 8 in Ref. [12]

$$\mathrm{d}N = n_\Omega(t) \, \mathrm{d} \ln \epsilon \, \mathrm{d}\Omega, \tag{2.3}$$

and for the particle number n_x in a differential logarithmic interval of radial distance to the shower axis $[\ln x, \ln x + \mathrm{d} \ln x]$, where $x \equiv \frac{r}{r_\mathrm{M}}$ and r_M is the Molière radius

$$\mathrm{d}N = n_x(t) \, \mathrm{d} \ln \epsilon \, \mathrm{d} \ln x. \tag{2.4}$$

The distributions are fully described in terms of relative evolution stage t

$$t = \frac{X - X_{\max}}{X_0}, \tag{2.5}$$

where the maximum number of particles is reached at slant depth $X_{\max}$ and $X_0 \simeq 36.7 \text{ g cm}^{-2}$ is the radiation length of electrons and positrons in air.

2.4 Electron-positron distributions

Given a shower profile $N(t)$ which describes the total number of particles at shower evolution stage t, we use Eqn. 2.4 to determine the number of particles in the differential intervals for distance r and energy ϵ: $N(t, \epsilon, r)$. Therefore the air shower is assumed to have a cylindrical symmetry and is binned in the following way: For a fixed energy range of $[\ln \epsilon, \ln \epsilon + \text{d} \ln \epsilon]$ the air shower is binned along the shower axis with bin width $\text{d}s$ (see Eqn. 2.1) perpendicular to the shower axis with radial bin width $\text{d}r$. The resultant cylindrical shells are then subdivided into N_ϕ equally spaced bins (so-called "voxels") over 2π around the shower axis (see Fig. 3). For each of these voxels, the energy-dependent number of particles is given by $N(t, \epsilon, r)/N_\phi$.
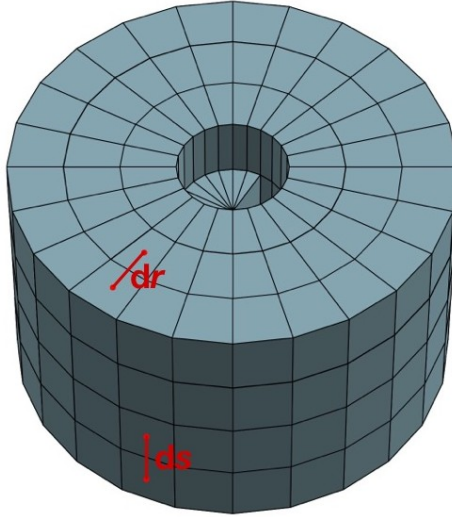

Figure 3: Schematic sketch of shower binning.

For an overview of the shower development, we show in Fig. 4a the distribution of electrons and positrons (integrated over the energy range of 1 MeV to 10 GeV) projected on the xz plane for a photon initiated air shower with zenith angle of 80°. One can clearly observe the shower axis together with the shower maximum at around $x \simeq 85 \text{ km}$ and $z \simeq 14 \text{ km}$.

The lateral distribution of shower particles around the shower axis will contribute to the production of Cherenkov light if their energy exceeds the energy threshold of $E_{Ch} \approx 50 \text{ MeV}$ at the position close to the shower maximum. In Fig. 4b, we compare the lateral distribution for particles emitting Cherenkov light ($\epsilon > E_{Ch}$) and those which will produce fluorescent light only ($\epsilon < E_{Ch}$). A large fraction (80 %) of the Cherenkov-light emitting particles are confined within 75 m while

fluorescent-light emitting particles are distributed over a larger distance: 80 % of these particles are located within 400 m to the shower axis.

(a)   (b)
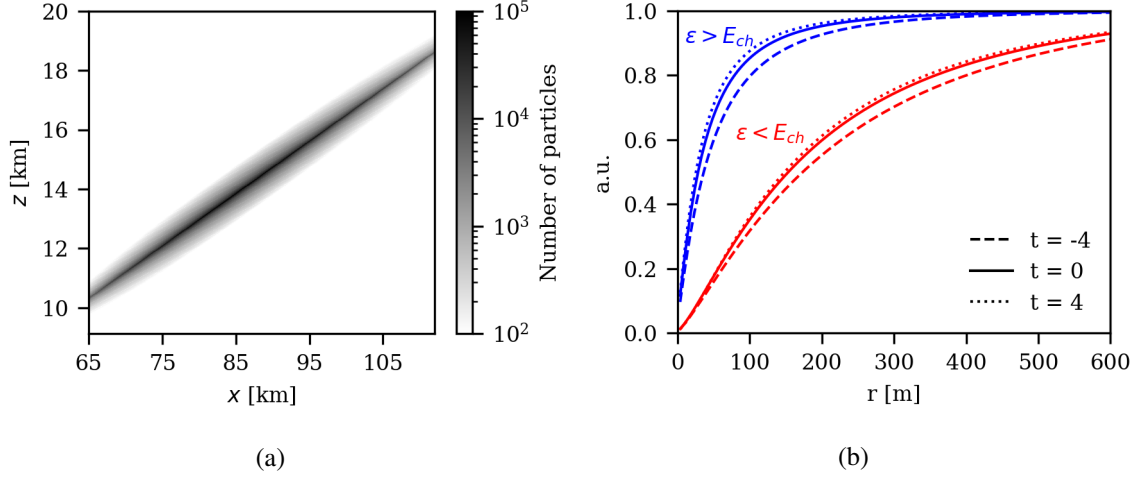
Figure 4: (a) Electron and positron distribution projected on the xz plane for a photon initiated air shower with primary energy of $E_\gamma = 975$ TeV at a zenith angle of 80°. (b) Normalized distribution of particle numbers as a function of distance to the shower axis at $t = -4, 0, 4$ for the same air shower as in 4a. E_{Ch} denotes the Cherenkov energy threshold. The maximum distance to the shower axis is set to 1 km.

## 2.5 Ionization energy deposit

Electrons and positrons deposit energy differently in collisions with air molecules when passing through the atmosphere [13]. The stopping power for electrons can be calculated with the Møller cross section and for positrons with the Bhabha cross section [14]. Both stopping power formulas including the parameter values used in this work can be found in [15]. The resulting ionization energy losses are assumed to be deposited at the midpoints of each voxel.

We can readily estimate the accuracy of the parametrization for the energy spectrum given in Eqn. 2.2 by calculating the energy deposit using the stopping powers for electrons and positrons and compare it with results obtained with CORSIKA (see Appendix A.1). In Fig. 5, we compare our results for the energy deposit per slant depth $\frac{\mathrm{d}E}{\mathrm{d}X}$ with CORSIKA for photon initiated air showers in the energy range of 900 TeV to 1000 TeV at a zenith angle of 70° and 80°. The number of individual air showers is ~ 850 per zenith angle. The relative error is calculated as

$$\text{rel. error} = \frac{(\mathrm{d}E/\mathrm{d}X)_{\text{EASpy}} - (\mathrm{d}E/\mathrm{d}X)_{\text{CORSIKA}}}{(\mathrm{d}E/\mathrm{d}X)_{\text{CORSIKA}}}.$$

One can observe that at early shower stages the relative difference is $\sim 5 - 10\%$ while at later stages the correspondence is better than 5% for both zenith angles. We found that deviations from the CORSIKA results mainly depend on the zenith angle, i.e., a slightly better correspondence at zenith angles around $\sim 70°$ compared to zenith angles closer to 80° and a negligible dependence on the primary particle energy.
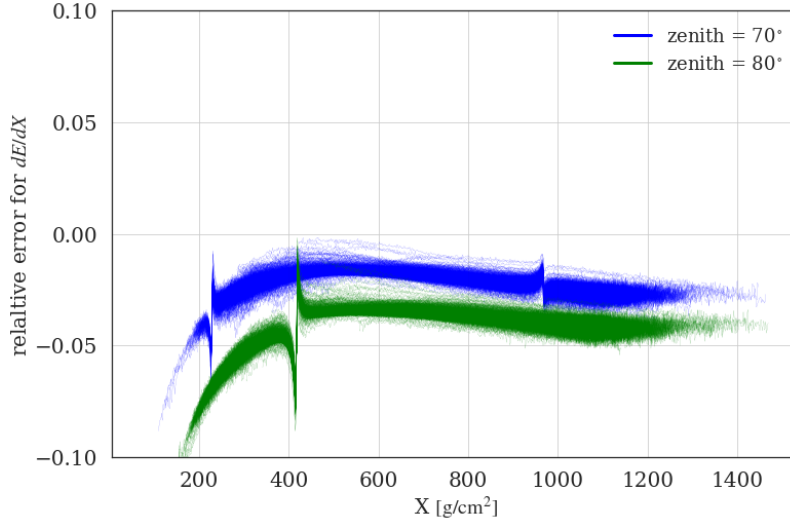
Figure 5: Relative error for the energy deposit per slant depth $\frac{dE}{dX}$ as a function of slanth depth X for photon initiated air showers with zenith angles 70° and 80°.

The "spikes" in Fig. 5 are related to the way the atmosphere is treated with `CORSIKA`: The "CURVED" option uses a "sliding plane atmosphere" instead of a fully spherical system. Every time the horizontal displacement of a particle exceeds a limit of 6 km to 20 km (depending on altitude), a transition to a new, locally plane atmosphere is performed [16]. Apparently this treatment introduces "spikes" whenever the transition is performed.

2.6 Fluorescence light

A fraction of the ionization energy deposited in the atmosphere (see 2.5) leads to the excitation of the nitrogen atoms with subsequent fluorescence light emission with a typical life time of the excited state of order ~ 40 ns (e.g. [17], [18]). The number of produced fluorescence photons N^{fl} per slant depth dX can be calculated with:

$$\frac{dN^{fl}}{dX} = N(t, \epsilon, r) \cdot Y_{air}(\lambda, T, p) \cdot \frac{dE}{dX}, \tag{2.6}$$

where $Y_{air}(\lambda, T, p)$ is the fluorescence yield in air depending on wavelength λ (in nm), ambient atmospheric pressure p and temperature T. This way, the amount of fluorescence light is directly proportional to the rate of ionization energy loss $\frac{dE}{dX}$. The fluorescence yield in air is usually expressed in terms of the absolute yield of the 337 nm band at reference pressure p_0 and temperature T_0:

$$\frac{Y_{air}(\lambda, T, p)}{Y_{air}(337, T_0, p_0)} = \frac{I_\lambda(T_0, p_0)}{I_{337}(T_0, p_0)} \cdot \frac{1 + p_0/p'_{337}(T_0)}{1 + p/p'_\lambda(T)},$$

where $I_\lambda(p_0, T_0)$ is the specific intensity and the function $p'_\lambda(T)$ takes into account temperature-dependent non-radiative de-excitation effects. The relative intensity I_λ/I_{337} (see Fig. 6) highlights

that most of the fluorescence lines are located at $\lambda \lesssim 400\,\text{nm}$. A detailed discussion on the temperature, humidity and pressure dependence of the air-fluorescence yield and the function $p'_\lambda(T)$ can be found in [19, 20]. The parameters used for the air-fluorescence yield are listed in Appendix B.

We assume that fluorescence emission is isotropic. Therefore, only a small fraction of the fluorescence photons will be observed by the telescopes. Instead of randomly distributing the photons over 4π and keeping track of each photon trajectory we assume that the amount of fluorescence photons N_{sphere}^{fl} hitting the telescope's sphere is given by its angular size seen from the position of a individual voxel. Consequently, the fraction N_{sphere}^{fl}/N^{fl} of the produced fluorescence photons hitting the telescope's sphere depends only on the ratio of its radius R and distance d to the voxel position:

$$
\begin{aligned}
\frac{N_{sphere}^{fl}}{N^{fl}} &= \frac{\Delta\Omega(d, R)}{4\pi} \\
&= \frac{1 - \sqrt{1 - R^2/d^2}}{2} \approx \frac{R^2}{4d^2}.
\end{aligned}
\tag{2.7}
$$

For a zenith angle of 70°(80°) and a radius $R = 14\,\text{m}$, the resulting fraction is $\approx 10^{-8}(10^{-9})$. This substantial decrease when going from 70° to 80° is a direct consequence of the fact that the distance of the telescope to the shower maximum increases rapidly with increasing zenith angle of the air shower.
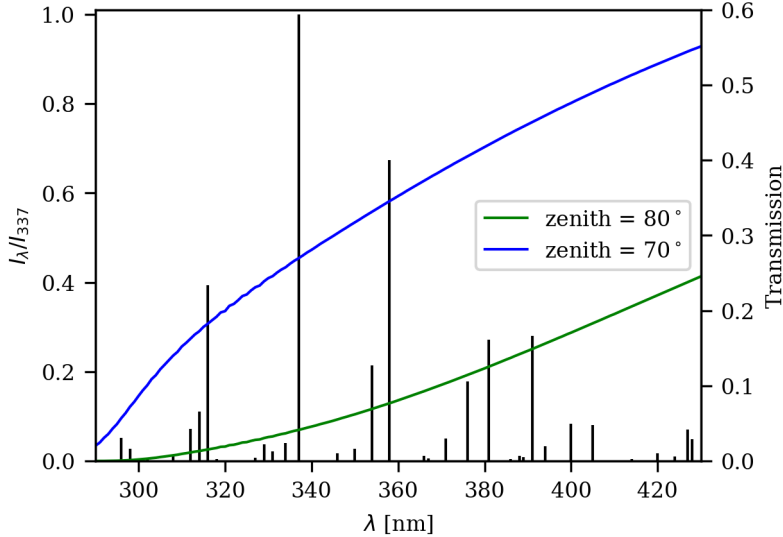
Figure 6: Black lines denote the wavelength dependent intensity relative to the 337 nm band I_λ/I_{337} (left axis). The blue(70°) and green(80°) lines describe the transmission from the position of the shower maximum down to the observation level (right axis).

In addition to the geometrical dilution of the fluorescence light, the atmospheric transmission decreases with increasing zenith angle (increasing slant depth). We compare the relative transmissivity for zenith angles of 70° and 80° in Fig. 6. The starting height is taken as the average height of the shower maximum of air showers with $E_\gamma \sim 1\,\text{PeV}$ (70°: $\sim 10\,\text{km}$ and 80°: $\sim 14\,\text{km}$). The

observation level is at a height of ~ 1.8 km asl. The majority of the produced fluorescence photons will have a wavelength $\lambda \lesssim 400$ nm. For a zenith angle of $80°$ only $\approx 4\%$ of the emitted light with wavelength $\lambda = 337$ nm will reach the observation level, while for $70°$ the observable light increases to $\approx 27\%$ of the emitted light.

2.7 Cherenkov light

The total number of Cherenkov photons N^{Ch} produced per slant depth dX between wavelength λ_1 and λ_2 by electrons with energy ϵ at relative evolution stage t and lateral distance to the shower axis r is given by

$$
\begin{aligned}
\frac{\mathrm{d}N^{Ch}}{\mathrm{d}X} = N(t, \epsilon > E_{Ch}, r) \cdot \frac{2\pi}{\alpha\rho(h)} \cdot \frac{\lambda_2 - \lambda_1}{\lambda_1\lambda_2} \\
\cdot \left(1 - \frac{1}{n^2(h)\beta^2}\right),
\end{aligned}
\tag{2.8}
$$

where E_{Ch} is the Cherenkov energy-threshold, α the fine-structure constant, $\beta = v/c$, and $n(h)$ the refractive index. The produced Cherenkov photons are emitted at the midpoint of the corresponding voxel positions.

The parametrization of the angular spectrum n_Ω (see Eqn. 2.3) is given in terms of the particle energy ϵ, which changes for different radii r. The resulting mean angle to the shower axis $\langle\theta_p\rangle$ is calculated using the expectation value of n_Ω as given by [12].

Commonly, the Cherenkov emission angle θ_{Ch} is assumed to be smaller than $\langle\theta_p\rangle$. However, for LZA observations, the increased threshold energy E_{Ch} leads to a reduced value of $\langle\theta_p\rangle$, such that for sufficiently large energies, the Cherenkov angle dominates and can not be neglected anymore. This is shown in Fig. 7 where the two angles are compared to each other. The average angle $\langle\theta_p\rangle$ reaches values similar to the Cherenkov angle at energies of $\epsilon = 400$ MeV $\ldots$ 500 MeV. Given that most electrons will emit Cherenkov light close to the threshold, it appears at first glance to be a good approximation to neglect the Cherenkov angle. However, even at energies close to threshold, the additional widening of the angular distribution of the emitted light through the Cherenkov angle leads to a substantial change of the order of a few 100 m on the impact position at the detector level.

Finally, the number of Cherenkov photons hitting the telescope's sphere N^{Ch}_{sphere} is calculated in the following way: For each voxel position and energy bin, the equation 2.8 is evaluated. The momentum vector of the emitting electrons is used to construct a plane which is perpendicular to its direction and intersects the midpoint of the telescope's sphere. This plane is consequently intersected by the Cherenkov cone and the telescope's sphere which define two circles (see Fig. 8). The possible two intersection points mark an arc of length L along the Cherenkov cone that is inside of the sphere. The fraction of photons intersecting the sphere's surface equals the fraction of the arc length:

$$
\frac{N^{Ch}_{sphere}}{N^{Ch}} = \frac{L}{2\pi r_{Ch}}.
\tag{2.9}
$$

This approach does not require any approximations and reduces the necessary computation time in comparison to e.g., ray-tracing approaches.
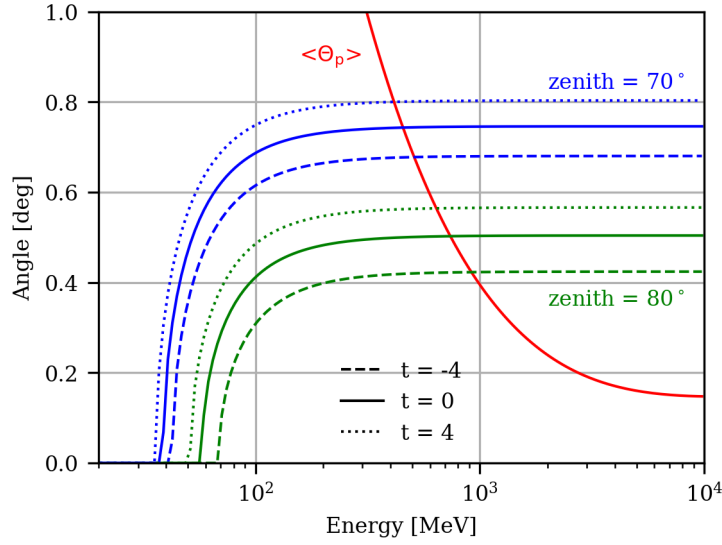
Figure 7: The red line marks the mean angle to the shower axis $\langle \theta_p \rangle$ of electrons as a function of energy. Blue and green lines indicate the Cherenkov emission angle for zenith angles of $70°$ and $80°$ respectively and for different stages of shower evolution ($t = -4, 0, 4$) marked by dashed, solid, and dotted lines.
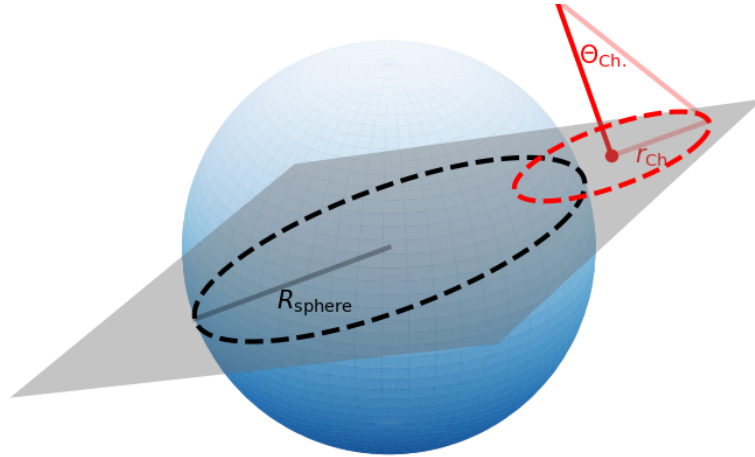
Figure 8: Thick red line is parallel to the momentum vector of the electrons, θ_{Ch} the Cherenkov angle and r_{Ch} is the radius of the Cherenkov circle in the intersecting plane (in grey).

3 Imaging of simulated air showers

So far, we have described how we calculate the total number of fluorescence and Cherenkov photons produced for each voxel position and how many of these photons (N_{sphere}^{fl}, N_{sphere}^{Ch}) will intersect the telescope sphere. In this approach, the directional vector of individual photons is not stored, such that the generation of a camera image requires a simplified treatment. To this end, we make use of the fact that the shower maximum is at a distance d of 50 km to 100 km which is much larger

than the radius of the sphere (e.g., for the largest Cherenkov telescope $R = 14$ m). We can therefore safely assume that all photons from a distant voxel intersect the sphere along its diameter. This approximation is justified for large distance d, such that the maximum angle difference $\Delta\alpha$ for a photon which is tangential to the sphere can be approximated

$$\Delta\alpha = \arctan\left(\frac{R}{d}\right) \approx R/d. \tag{3.1}$$

For the large zenith angles considered here, $d \gtrsim 50$ km, such that $\Delta\alpha \lesssim 0.016°$. The resulting widening of the angular distribution of photons intersecting the sphere is smaller than the typical angular field of view of individual pixels and can therefore be neglected (the smallest pixel currently used covers a patch in the sky with a diameter of $0.07°$ [21]). This way, the resulting computation time can be reduced by more than three orders of magnitude in comparison to a ray-tracing approach. An obvious downside of this method is that the approximation leads to a systematic underestimate of the image width for the shower tail which even at large zenith angles is observed at a distance of 10 km to 20 km. For a combination of a very large telescope with a very high-granular camera, the paraxial approximation introduced breaks down. Conversely, at smaller zenith angles, the images generated with the paraxial approximation will be only accurate for small-sized telescopes. This caveat requires an individual consideration for each combination of telescope radius, zenith angle, and pixel size.

As a final step towards generating realistic camera images which are based on the number of photo-electrons detected in the individual pixels, we implement a coarse simulation of the detection process which includes:

- the combined wavelength-dependent quantum efficiency of the photo-cathode and collection efficiency for photo-electrons,

- the wavelength-dependent mirror reflectivity of the mirror facets, and

- the wavelength-dependent transmittance of the camera protective cover.

Additionally the user can provide a single value for all wavelengths which takes into account shadowing effects of the camera support structure and the light guide efficiency of the PMT.

Therefore, in order to take into account the aforementioned wavelength-dependent effects in addition to atmospheric transmission, we pre-compute for each voxel with index j at a given height $h(j)$ above ground the probability P_j for a photon (fluorescence or Cherenkov) to be detected after propagating through the atmosphere. The probability is calculated by integrating the product of emissivity $\Lambda^{Ch,fl}(\lambda)$, detection efficiency $\eta(\lambda)$, and transmission $T(\lambda, h)$. The result is normalized to obtain a probability:

$$P_j = \frac{\int_{\lambda_1}^{\lambda_2} \Lambda^{Ch,fl} \cdot T(\lambda, h)\eta(\lambda) \, d\lambda}{\int_{\lambda_1}^{\lambda_2} \Lambda^{Ch,fl} \, d\lambda}. \tag{3.2}$$

The wavelength distribution for the fluorescence photons is given by the wavelength dependent intensity relative to the 337 nm band (see Fig. 6) and Cherenkov photons are following a $1/\lambda^2$ distribution.

The point spread function of the camera is characterized by external lookup-tables with the 68% containment radius as a function of off-axis angle and zenith angle. The night sky background (NSB) can be simulated by providing an average background rate in units of photo-electrons per nanosecond and per pixel. The detector simulation does not take into account more specific effects related to electronics, for example formation of a trigger, non-linearities and digitization effects in the read-out. This can be in principle included in this framework or other existing packages like `simtel_array` [22] can be used to obtain a more specific and accurate simulation of the detector response.
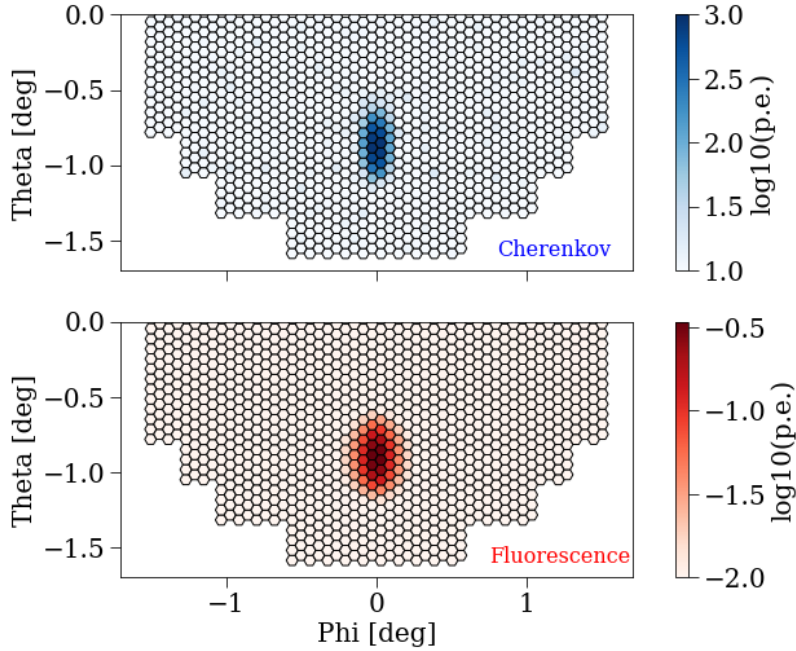
Figure 9: Example camera image formed by Cherenkov (upper panel) and fluorescence light (lower panel) generated by an air shower with $E_\gamma = 780$ TeV at a zenith angle of 80°. Note, the logarithmic scales differ between the two images.

The resulting image is shown in Fig. 9 formed by Cherenkov (upper panel) and fluorescence light (lower panel) emitted by an gamma-ray air-shower with an energy of $E_\gamma = 780$ TeV at a zenith angle distance of 80°. As expected and well-known from observations of air Cherenkov light with Cherenkov telescopes, the resulting image resembles an ellipse with a major axis (so-called *length*) which is roughly three times as large as the minor axis (so-called *width*). The fluorescence light image looks very similar to the Cherenkov light image, albeit with a peak intensity reduced by a factor of ≈ 3000. Furthermore, the fluorescence light image is of similar length, but noticeably larger width than the Cherenkov light image. This is mainly a consequence of the fact that Cherenkov emission does have an energy threshold E_{Ch} and that the majority of the particles with $\epsilon > E_{Ch}$ are very close to the shower axis (see Fig. 4b). Contrary, fluorescence emission scales with deposited

energy and also electrons which are further away from the shower axis with $\epsilon < E_{Ch}$ will therefore produce fluorescence photons. Additionally, fluorescence emission is isotropic while Cherenkov emission does have an opening angle θ_{Ch} which limits the visibility of the shower for an IACT.
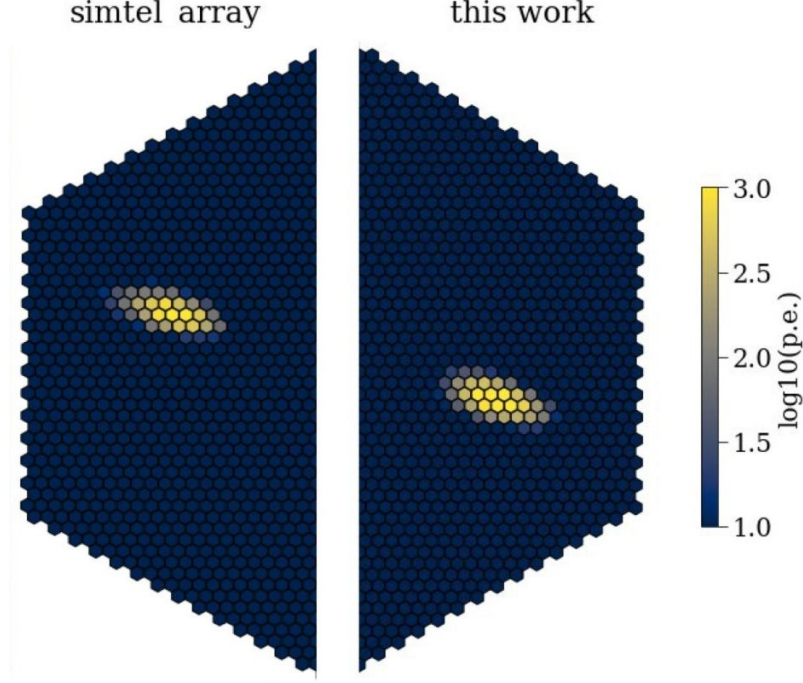
Figure 10: Side-by-side comparison of the camera image for a shower with zenith angle of $80°$ obtained with `simtel_array` (left) and `EASpy` (right). The `simtel_array` camera image is rotated by $180°$.

4 Verification with a full simulation

Finally, we present an example for a shower image in Fig. 10 and compare it side-by-side with the shower image as calculated with a complete air-shower simulation (see Section A.1) and ray-tracing for Cherenkov-light using the `sim_telarray` package (see Section A.2). In order to make the comparison meaningful, we have included the limited dynamical range and saturation of pixel amplitudes similar to `sim_telarray`.

Note, that the underlying shower profile is identical for both images. The side-by-side comparison demonstrates that even with the simplifications introduced above and the coarse detector simulation used here, the images appear quite similar. The position of the image in the camera, the light recorded in the pixels are in good agreement with each other. The approximate length matches between the two images, while the width appears slightly larger for `EASpy`. This is readily explained by the assumption of a symmetric PSF of the telescope optics. However, the PSF is in general elongated along the radial direction which leads to a smaller apparent width of the registered image.

To make the comparison more quantitative, we consider a larger sample of simulated air showers presented in Fig. 15a and compare the resulting distributions of width(length) of the images for

zenith angles of 70° and 80°.

4.1 Width distribution

In Fig. 11a, the image width obtained with the full simulation (w_s) is compared with the results of EASpy (w) for a zenith angle of 70° and 80°. The two-dimensional histogram for a zenith angle of 70° indicates a clear and linear correlation between w_s and w. The average values as well as the individual distributions are very similar. The blue (70°) and green (80°) ellipses mark the 68 %ile boundary around the centroid of the distribution. For each of the two zenith angles, the orientation and position of the ellipses match well between the two methods. The noticeable differences are most likely related to differences in the cleaning procedures that have not been applied in an identical way for the two methods. As expected, the width observed at 80° is systematically smaller than observed at 70°, because of the increased distance to the shower maximum.
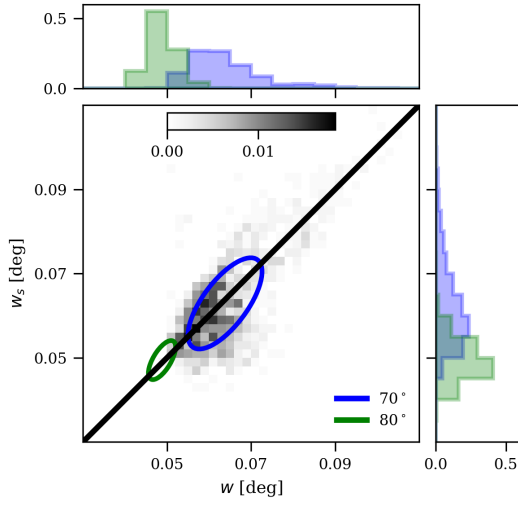
(a) Comparison of width parameter for showers with zenith angle 70°(80°) between sim_telarray (w_s along y-axis) and EASpy (w along x-axis). The 2D histogram is plotted only for 70° for visibility. The blue(green) ellipse describes the 68% enclosure around the mean value. Top and right panel shows the projection of the w and w_s-axis respectively. The black line marks the identity $w = w_s$.
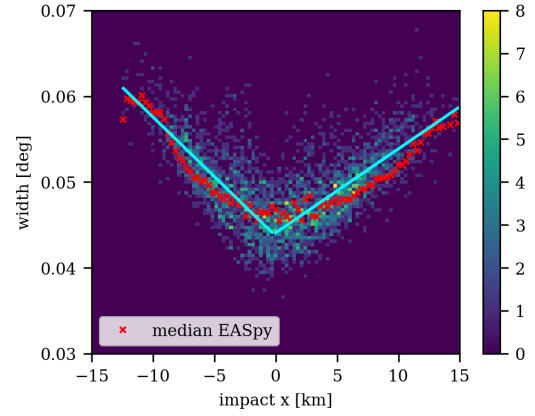
(b) Comparison of width parameter as a function of impact x-position for showers with zenith angle 80° between sim_telarray and EASpy. The 2D histogram shows only the values generated with sim_telarray, the red crosses mark the median values obtained with the EASpy, and the solid lines are derived by fitting a linear function to the median values of sim_telarray for $x \gtrsim 0$ and $x \lesssim 0$ respectively.

Figure 11: Comparison of width parameter between EASpy and sim_telarray.

The excellent agreement between the width w predicted with the simplified approach in EASpy and the full simulation encourages further comparison between image parameters seen at various distances of the telescope from the shower impact position. In Fig. 11b, we compare the width values for shower impact positions at zenith angle of 80° along the x-coordinate in the observation plane. The telescope is located at $x = y = 0$ and the shower moves from right to left. The 2D histogram shows the distribution of w_s while the red crosses are the median values of the w-distribution for slices in x. For ease of comparison, the cyan line from a linear fit to the w_s distribution is overlaid.

One can clearly observe consistently for both simulations, that with increasing distance d_{impact} of the telescope position to the impact position of the shower, the width value gets *larger*. At first glance, this appears counter-intuitive since with increasing d_{impact} the shower should appear *smaller*. However, from a geometrical point of view, the telescope will only register photons with a larger angle with respect to the shower axis for increasing distance d_{impact}. Consequently, the light observed at these distances is emitted from electrons with large $\langle \theta_p \rangle$ which on average also have a larger distance to the shower axis.

The absolute value of the slope of the solid lines in Fig 11b seems to be smaller for $x \gtrsim 0$ compared to $x \lesssim 0$. This can be explained by considering that for $x \gtrsim 0$ the shower maximum is further away from the telescope position compared to $x \lesssim 0$ and therefore the shower is observed under smaller angles.

Given these explanations, it is remarkable that the parametrization of the shower angle and its dependence on the radial distance to the shower axis is sufficiently accurate to capture the interesting property of increasing width with increasing distance to the observer.

4.2 Length distribution

The distribution of image length is shown in Fig. 12a for the two considered zenith angles of 70° in blue and 80° in green. Overall, the distributions for both zenith angles are in good agreement considering the simplified approach. The modest tilt in the orientation of the blue ellipse is caused by a tail of images reconstructed with $l_s \gtrsim 0.18°$ for the `sim_telarray` distribution. The apparent tilt of the green ellipse highlights the larger values of l_s found for $l \lesssim 0.11°$. This slight deviation is related to the differences in the image cleaning. Within `sim_telarray`, pixels are removed with amplitudes below a threshold set relative to the brightest pixel whereas in EASpy no imaging cleaning is applied (see for a comparison of uncleaned images Appendix A.2). Similar to the width distribution, the average value of the length becomes smaller for larger zenith angle distances.

Similar to the presentation of the width parameter in the previous subsection, we compare the apparent length of the images recorded at different positions of the shower core in the observer plane. The result is shown in Fig. 12b for a zenith angle of 80°. As before, the red crosses mark the median values obtained with `EASpy` and the overlaid solid lines characterize the median values of `sim_telarray`.

The conclusions are quite similar to Fig. 11b: for large d_{impact} the telescope will only register photons with a large angle with respect to the shower axis leading to an increase of the resulting length parameter. This picture holds as long as the shower is fully captured inside the camera field of view. Once the shower images are getting cut off at the camera edges the length values start to drop (see in Fig. 12b for $x \lesssim -9\,\text{km}$ and $x \gtrsim 10\,\text{km}$). The close agreement between l and l_s demonstrates the validity of the simplified approach regarding the longitudinal development of the air shower.

A key difference between Fig. 11b and Fig. 12b is the more uniform spread of values found for any given x: While for Fig. 11b the difference between the maximum and minimum width value for $x \approx 0$ is $\sim 0.01°$, the corresponding difference for the length value in Fig. 12b is roughly 10 times higher ($\sim 0.1°$). Upon closer inspection, the spread relates to a systematic increase of the length with increasing distance along the y-axis for a fixed value of x. The obvious explanation is the
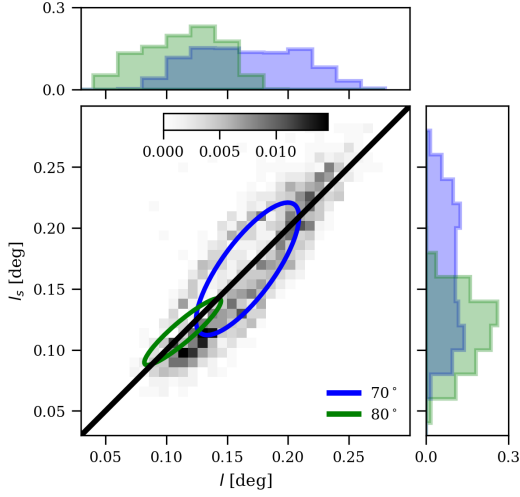
(a) Comparison of length parameter for showers with zenith angle 70°(80°) between `sim_telarray` (l along y-axis) and `EASpy` (l_s along x-axis). The 2D histogram is plotted only for 70° for visibility. The blue(green) ellipse describes the 68% enclosure around the mean value. Top and right panel show the projections of the l and l_s-axes respectively. The black line marks the identity $l = l_s$.
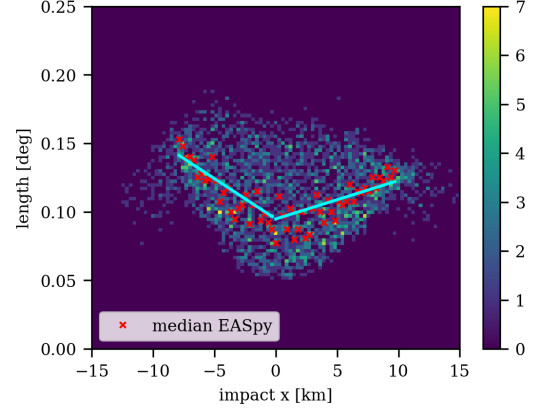
(b) Comparison of length parameter as a function of impact x-position for showers with zenith angle 80° between `sim_telarray` and `EASpy`. The 2D histogram shows only the values generated with `sim_telarray`, the red crosses mark the median values obtained with the `EASpy`, and the solid lines are derived by fitting a linear function to the median values of `sim_telarray` for $x \gtrsim 0$ and $x \lesssim 0$ respectively.

Figure 12: Comparison of length parameter between `EASpy` and `sim_telarray`.

longitudinal development of the shower captured in the length parameter while the width parameter is mainly sensitive to the shower maximum.

5 Photon ground distribution

So far, we have considered the Cherenkov-light images recorded by a telescope observing the shower with its optical axis aligned parallel to the shower axis. In addition to the Cherenkov light, fluorescence is emitted isotropically and can be observed under arbitrary angles with respect to the shower axis such that the apparent brightness scales with the inverse of the distance squared to the shower maximum. At small zenith angles, the maximum photon density of fluorescence and Cherenkov light coincide.

At larger zenith angles, these positions are displaced with respect to each other. This can be seen in Fig. 13 where both, the photon density of fluorescence and Cherenkov light on the ground (ground level is at a height of 1.8 km) are shown on a grid covering an area of $16\,000\,\text{km}^2$ for an air shower with $E_\gamma = 10\,\text{PeV}$ at 80°. The atmospheric absorption for Cherenkov(fluorescence) photons is treated in a simplified way: we calculate the average absorption from the position of the shower maximum to the ground level for a photon path with zenith angle 80°(0°) and apply this factor to all Cherenkov(fluorescence) photons. The two peak positions are displaced by $\approx 80\,\text{km}$. The peak position of the air fluorescence light pool is close to the projected position of the shower maximum
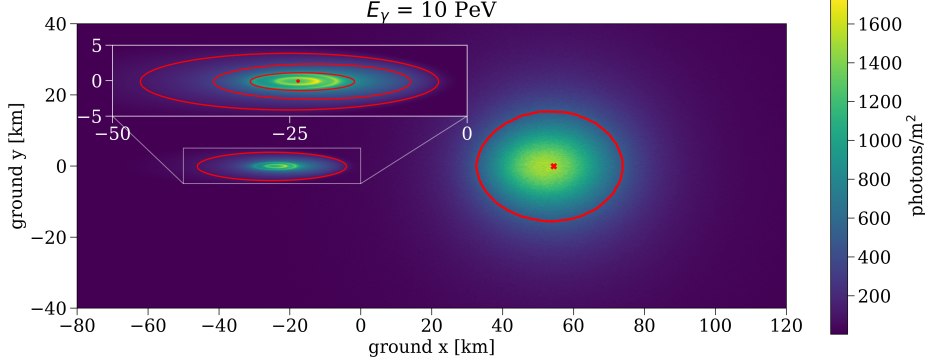
Figure 13: Cherenkov and fluorescence photon ground distribution for an air shower with zenith angle 80°. The fluorescence photon density is up-scaled by a factor of 5 to match the Cherenkov photon density. The red lines mark an iso-contour at a level of 100 photons/m^2 (here the fluorescence density is not up-scaled). Red cross marks the position of the shower maximum. Inset axis: Zoomed-in version of Cherenkov photon ground distribution. The dot marks the position of the impact, red lines indicate the iso-contours at a level of 100 photons/m^2, 350 photons/m^2 and 700 photons/m^2.

and the peak position of the Cherenkov light pool is close to but not identical with the shower core position on the ground.

The red ellipses indicate iso-contours of photon surface density of 100 photons/m^2. In this context, it is important to note, that at large zenith angles, there is no noticeable contamination of Cherenkov light by fluorescence light. This effect has been studied in [6] for a zenith angle of 30°, where the authors show that at distances ∼ 1 km from the impact point 45 % of the light registered at PeV energies with a wide-angle detector would be atmospheric fluorescence emission.

While the circular shape of the iso-contour for the fluorescence photon surface density reflects the isotropic nature of fluorescence emission, the iso-contour for the Cherenkov case is elongated in the x-direction by orders of magnitude compared to the y-direction. The inset-axis of Fig. 13 shows a zoomed-in version of the Cherenkov photon ground distribution, with three isocontours (at 100, 350, and 700 photons/m^2) highlighting its complex structure. Close to the impact position, the two ring-like structures are directly related to the minimum and maximum Cherenkov-angle θ_{Ch} of the superposition of the Cherenkov light emission from the entire shower development. Beyond the outer ring feature, the photon density drops quickly since this emission is produced mainly be electrons from the later shower development with a large angle with respect to the shower axes. This drop is more pronounced for light hitting the ground on the far side of the impact position (in the figure to the left). This is explained by the geometrical effect of projecting the photon density to the ground (see Fig. 14).

6   Summary

In this work, we have presented a framework for
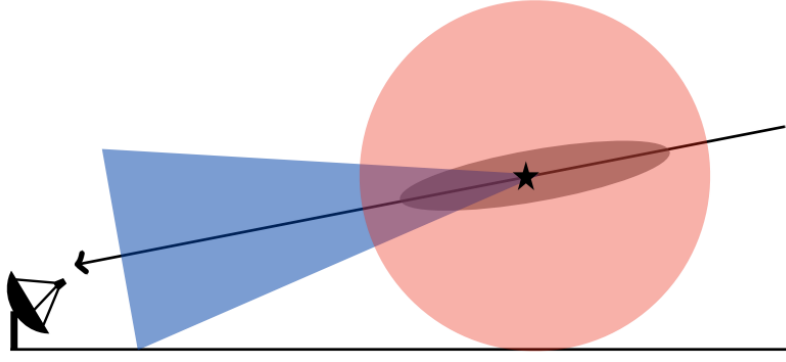
Figure 14: Sketch of the geometry properties for Cherenkov and fluorescence emission. The black star marks the shower maximum, the blue shaded area the Cherenkov emission cone and the red shaded area denotes isotropic fluorescence emission. The black line describes the shower axis and the arrow the direction of propagation of the shower.

- a three-dimensional simulation of extended air showers at large zenith angles,

- the consequent emission of fluorescence and Cherenkov light,

- and the imaging of the simulated air showers.

The three-dimensional simulation of the air shower makes use of parametrizations for electron-positron distributions for particle energy, angular spectrum and lateral distance [12]. Additionally, we assume that these particles are distributed homogeneously around the shower axis such that the simulated air shower follows a cylindrical symmetry.

For the zenith angle range discussed in this work (70° to 80°), the commonly used approximation of a plane-parallel atmosphere is not applicable anymore. Therefore, we assume a spherical atmosphere in order to accurately calculate the traversed mass density and the corresponding atmospheric parameters along the path of the primary particle. In this framework, we compute the emission of fluorescence and Cherenkov light in an analytical way on the basis of Møller(Bhabha) cross section and the Frank–Tamm formula respectively. In this context we note, that at LZA, the Cherenkov emission angle is generally larger than the mean angle of electrons/positrons to the shower axis and needs to be included in the calculation.

The amount of light reaching the detector level after Rayleigh- and Mie-scattering as well as ab-sorption processes is determined by using pre-computed lookup-tables generated with the `MODTRAN` program. A simple plane parallel atmosphere model, where the optical depth scales with the secant of the zenith angle, would underestimate the transmission by $\sim 10\%$. Full simulations of Cherenkov and fluorescence photons generated by the particles in the air shower are demanding in terms of computational time and memory required. Here, we have introduced a novel approach where the number of photons detected with a telescope are determined with geometrical reasoning. As we have demonstrated, this approach is accurate for LZA observations and reduces the computational time considerably.

In order to verify the approach presented here, we compare the width(length) parameter of Cherenkov air-shower images at zenith angle 70° and 80° between `EASpy` and `sim_telarray`. We

find for these most relevant imaging parameters very good agreement for the entire zenith angle range considered. This is remarkable since the computation time of `EASpy` does not scale with the energy of the primary particle. In this way, `EASpy` provides a fast and flexible approach to simulate a large number of air showers and the resulting images recorded with various Cherenkov telescope arrays. Specifically, for the so-far unexplored energy beyond 100 TeV, it is possible to simulate and optimize the sensitivity and performance of these arrays.

The `EASpy` framework provides additionally insights into the generation of air shower images as well as the distribution of light in the detector plane. We have found that air shower images appear wider and longer with increasing impact distance, an effect that has previously not been noted. This apparent increase is related to the interplay of the Cherenkov angle and the average angle of shower particles with respect to the shower axis. The effect is confirmed in the detailed simulations using `CORISKA/sim_telarray`. The distribution of light on the ground calculated with `EASpy` shows clear separation between the Cherenkov and fluorescence light pools. This can not be investigated with the standard `CORSIKA` framework. These features may offer opportunities for observations in future work. Our framework will be released in the near future for general usage.

Acknowledgement

A   Standard Monte Carlo simulations for imaging Cherenkov telescopes

A.1   Air shower simulations with `CORSIKA`

The widely used `CORSIKA` [23] framework for air shower simulations has been established as the standard software in the field of ground-based air shower detection. The underlying Monte Carlo approach has been used in this context since at least 50 years [24]. CORSIKA combines the treatment of hadronic and electromagnetic interactions using state-of-the art interaction models that have been verified with experimental data obtained at the highest energy with the large hadron-collider (LHC) [25]. The electromagnetic cascade is computed using the well-established EGS-4 code [26]. The CORSIKA code includes radiative processes like Cherenkov light generation. Other processes like radio or fluorescence emission are not included in the official release.

In `CORSIKA` charged particles are tracked as they undergo possible interactions or decay, multiple scattering, bending of the trajectory in the Earth's geomagnetic field, and ionization energy losses, as long as the particle survives a user defined angular and energy cut.

For the Cherenkov light production each track segment of a charged particle is divided into smaller sub-steps such that in each sub-step one photon *bunch* is emitted at the midpoint of the sub-step. The number of Cherenkov photons in one bunch is given by the user defined *bunchsize* which defines the number of sub-steps needed until the number of Cherenkov photons in one bunch is less than the defined bunchsize. For our simulation, we set the *bunchsize* to five photons which is a

compromise between resolution and computation time required. For the typical detection efficiency of ≈ 10 % for ground-based detection, less than one photon would be detected per bunch.

At each step, the number of produced Cherenkov photons and the emission angle is determined by the height-dependent refractive index and velocity of the charged particle, while assuming a continuous energy loss along its path. Within the IACT package for CORSIKA, telescopes are modelled as spheres with adjustable position and radius for each telescope. The bunches are transported to ground level and for those intersecting a telescope sphere, all relevant informations are stored in a file. Additionally, CORSIKA provides the option to count the number of particles passing through intervals of slant depth and their energy deposit for various particle groups (γ, $e^{\pm}$, $\mu^{\pm}$, hadrons, Cherenkov photons) This information is written to a separate file.

In this work we used CORSIKA (v7.7402) to obtain shower profiles for photon air showers with energies in the range of 100 TeV to 1000 TeV and zenith angles between 70° and 80° in steps of 2°.

The resulting shower profiles are used for calculating the electron-positron distributions for particle energy, angular spectrum and lateral distance (see Section 2.3). For each zenith angle, we simulated $\sim 8\,000$ showers which sums up to a total of $\sim 50\,000$ showers (see Fig. 15a).

The corresponding mean shower profile per energy of the primary photon for each zenith angle bin is shown in Fig. 15b. The shower profiles are described in terms of the relative evolution stage t (see Eq. 2.5). While the shower profiles converge at very early ($t \leq$ -4) and late stages ($t \geq 4$), they surprisingly deviate around the shower maximum ($t \sim 0$). This behavior is not seen, if the shower profiles are normalized to the number of particles at the shower maximum N/N_{max}, with $N_{\mathrm{max}} = N(t = 0)$.
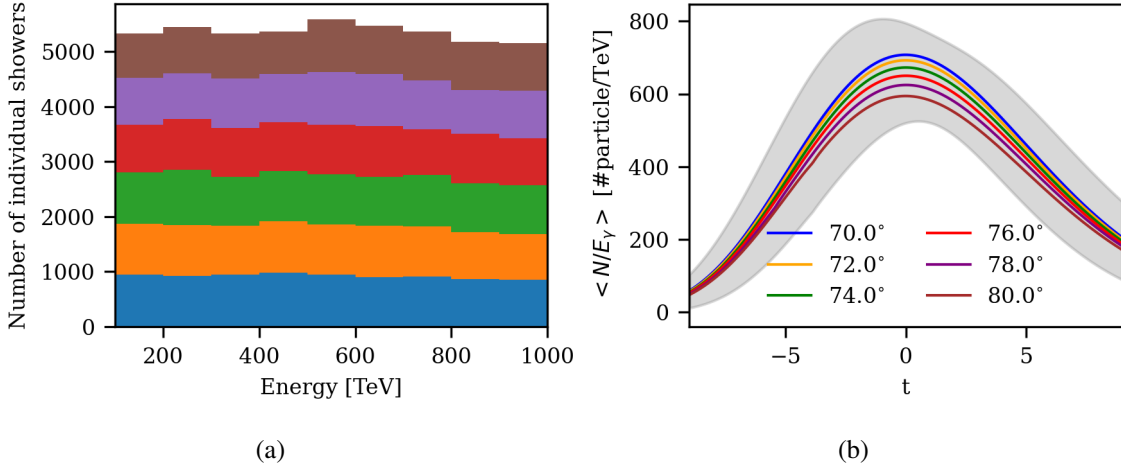
Figure 15: (a) Histogram of simulated showers with bin width of 100 TeV for each zenith angle. (b) Mean number of particles per primary gamma energy for each zenith angle bin. The gray shaded area denotes the envelope of the 1 σ error bands of zenith angle bins.

In the following, we provide all relevant information regarding CORSIKA version, compiling options, and parameter settings used to simulate the air showers:

CORSIKA version 7.7402

compiling options VOLUMEDET, IACT, ATMEXT, CURVED, VIEWCONE, SLANT, CERENKOV

interaction models QGSJET-01D [27], GHEISHA 2002d [28], EGS4 [26]

atmosphere all-year average profile at H.E.S.S. site

For the energy cut-off of the particle kinetic energy for hadrons, muons and electrons we used 0.3 GeV, 0.1 GeV and 0.001 GeV respectively. The lower and upper limit of the wavelength band for the Cherenkov radiation production covers a range 250 nm to 700 nm with a bunchsize of 5. The longitudinal development of particle numbers and energy deposit by ionization energy losses are sampled in steps of 2 g/cm^2. Explanations for the compiling options and keywords for the `CORSIKA` input card can be found in [16].

### A.2   Detector simulation with sim_telarray

The shower simulation as described in the previous section provides the information on the Cherenkov light received by a telescope located in the center of the so-called telescope sphere. The subsequent treatment of the different components of a telescope require a dedicated simulation. Since this simulation requires in-depth and specific details of the telescope hardware, it has often been treated by custom codes that are limited to a single experiment. In the past decade, `sim_telarray` [22] has been used for the HEGRA, H.E.S.S., and planned CTA IACT systems.

With the `sim_telarray` package each telescope of an IACT system can be configured individually. The photon information stored by CORSIKA are read-in and the atmospheric transmission defined by an external look-up table is applied to the photon bunches. Using ray-tracing, the remaining Cherenkov light is followed through the various optical components, until it converts into a photo-electron on the photocathode. The optical components can be configured in a flexible way to take into account the geometry of the mirrors, their alignment as well as the overall layout of the camera to include shadowing effects of masts etc. The efficiencies for reflection, absorption, and conversion are treated in a wave-length dependent way. The pulse-shape, after-pulsing, relative timing, triggering, and digitization can be fine-tuned with various parameters to match the actual setup. In addition to the Cherenkov light, the night-sky background is included as a noise source to the camera images.

Information about the position and number of photo-electrons for every pixel enables geometrical reconstruction of the shower using the classical Hillas parameters technique. While the `sim_telarray` package itself does not provide any reconstruction steps which involve look-up of other simulation data, e.g. gamma-hadron separation, it does provide a Postscript-generator for visualisation of the data, which includes the moments of the Hillas ellipse and the reconstructed shower direction.

As mentioned in section 4.2, `sim_telarray` applies a cleaning procedure in order to remove photo-electrons from the night sky background and electronics. This procedure will also inevitably remove photo-electrons produced by Cherenkov-photons. The small effects of the cleaning procedure can be observed by comparing Fig. 12a with Fig. 16, where in Fig. 16 the uncleaned images (i.e. only the photo-electrons produced by Cherenkov-photons) from `sim_telarray` were used.
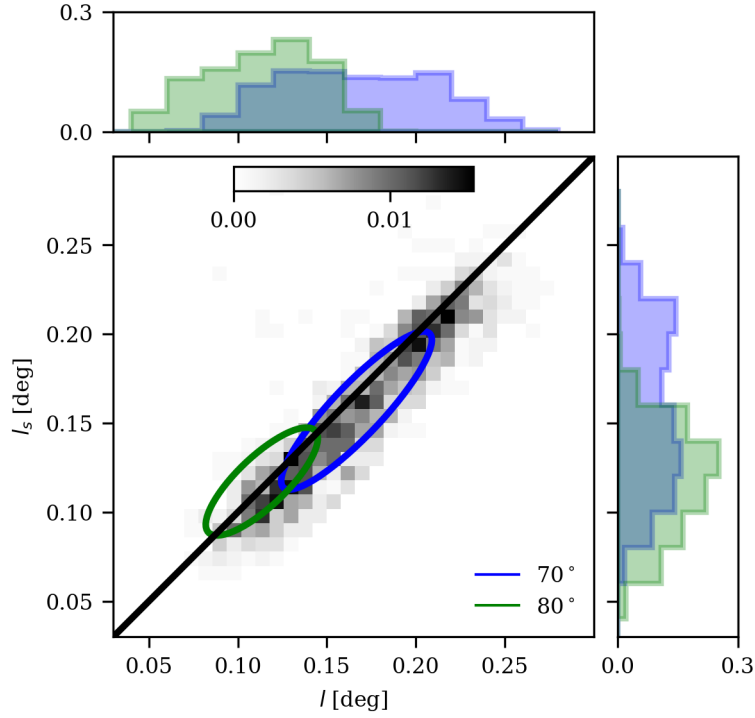
Figure 16: Same as in Fig. 12a but here using the uncleaned images from `sim_telarray`.

B Fluorescence parameters

In Table 2 we provide all necessary parameter values in order to evaluate $Y_{air}(\lambda, T, p)$ in Eq. 2.6. The parameter values are taken from [19], [20] and `ShowerModel`.

Table 2: Parameters for Fluorescence model. Reference atmospheric conditions for dry air are $p_0 = 800.0$ hPa and $T_0 = 293.0$ K. The table describes from left to right: wavelength λ in units of nm, relative intensity of each wavelength at reference atmospheric conditions, quenching pressure of dry air $PP0$ and quenching pressure of water vapor PPw in units of hPa and a parameter a which takes into account the temperature dependence.

λ	$\frac{I_\lambda(T_0,p_0)}{I_{337}(T_0,p_0)}$	$PP0$	PPw	a
nm	$\times 10^{-2}$	hPa	hPa	-
296	5.16	18.50	0.00	0.00
298	2.77	17.30	0.00	0.00
302	0.41	21.00	0.00	0.00
308	1.44	21.00	0.00	0.00
312	7.24	18.70	0.00	0.00
314	11.05	12.27	1.20	-0.13
316	39.33	11.88	1.10	-0.19
318	0.46	21.00	0.00	0.00
327	0.80	19.00	0.00	0.00

329	3.80	20.70	0.00	0.00
331	2.15	16.90	0.00	0.00
334	4.02	15.50	0.00	0.00
337	100.0	15.89	1.28	-0.35
346	1.74	21.00	0.00	0.00
350	2.79	15.20	1.50	-0.38
354	21.35	12.70	1.27	-0.22
358	67.41	15.39	1.30	-0.35
366	1.13	21.00	0.00	0.00
367	0.54	19.00	0.00	0.00
371	4.97	14.80	1.30	-0.24
376	17.87	12.82	1.10	-0.17
381	27.20	16.51	1.40	-0.34
386	0.5	19.00	0.00	0.00
388	1.17	7.60	0.00	0.00
389	0.83	3.90	0.00	0.00
391	28.00	2.94	0.33	-0.79
394	3.36	13.70	1.20	-0.20
400	8.38	13.60	1.10	-0.20
405	8.07	17.80	1.50	-0.37
414	0.49	19.0	0.00	0.00
420	1.75	13.80	0.00	0.00
424	1.04	3.90	0.00	0.00
427	7.08	6.38	0.00	0.00
428	4.94	2.89	0.60	-0.54

References

[1] L. Dirson and D. Horns, *Phenomenological modelling of the Crab Nebula's broadband energy spectrum and its apparent extension*, *A&A* **671** (2023) A67 [2203.11502].

[2] M. Actis, G. Agnetta, F. Aharonian, A. Akhperjanian, J. Aleksić, E. Aliu et al., *Design concepts for the Cherenkov Telescope Array CTA: an advanced facility for ground-based high-energy gamma-ray astronomy*, *Experimental Astronomy* **32** (2011) 193 [1008.3703].

[3] P. Sommers and J.W. Elbert, *Ultra-high-energy gamma-ray astronomy using atmospheric Cerenkov detectors at large zenith angles*, *Journal of Physics G Nuclear Physics* **13** (1987) 553.

[4] M. Collaboration, *MAGIC very large zenith angle observations of the crab nebula up to 100 tev*, *Astronomy & Astrophysics* **635** (2020) A158.

[5] V. de Souza, H. Barbosa and C. Dobrigkeit, *A monte carlo method to generate fluorescence light in extensive air showers*, *Astroparticle Physics* **22** (2004) 263.

[6] D. Morcuende, J. Rosado, J. Contreras and F. Arqueros, *Relevance of the fluorescence radiation in VHE gamma-ray observations with the cherenkov technique*, *Astroparticle Physics* **107** (2019) 26.

[7] K. Greisen, *Cosmic Ray Showers*, *Annual Review of Nuclear and Particle Science* **10** (1960) 63.

[8] T.K. Gaisser and A.M. Hillas, *Reliability of the Method of Constant Intensity Cuts for Reconstructing the Average Development of Vertical Showers*, in *International Cosmic Ray Conference*, vol. 8 of *International Cosmic Ray Conference*, p. 353, Jan., 1977.

[9] K. Kamata and J. Nishimura, *The Lateral and the Angular Structure Functions of Electron Showers*, *Progress of Theoretical Physics Supplement* **6** (1958) 93.

[10] F. Nerling, J. Blümer, R. Engel and M. Risse, *Universality of electron distributions in high-energy air showers—description of cherenkov light production*, *Astroparticle Physics* **24** (2006) 421.

[11] F.K. et al., *The MODTRAN 2/3 Report and LOW-TRAN 7 Model*, Phillips Laboratory, Hanscom AFB, MA 01731, USA (1996).

[12] S. Lafebre, R. Engel, H. Falcke, J. Hörandel, T. Huege, J. Kuijpers et al., *Universality of electron–positron distributions in extensive air showers*, *Astroparticle Physics* **31** (2009) 243.

[13] S.M. Seltzer and M.J. Berger, *Evaluation of the collision stopping power of elements and compounds for electrons and positrons*, *The International Journal of Applied Radiation and Isotopes* **33** (1982) 1189.

[14] E.A. Uehling, *Penetration of heavy charged particles in matter*, *Annual Review of Nuclear Science* **4** (1954) 315 [https://doi.org/10.1146/annurev.ns.04.120154.001531].

[15] P.D. Group, *Particle physics booklet*, 2022.

[16] T.P. D. Heck, *Extensive air shower simulation with corsika: A user's guide, version 7.7410*, 2021.

[17] F. Arqueros, F. Blanco and J. Rosado, *Analysis of the fluorescence emission from atmospheric nitrogen by electron excitation, and its application to fluorescence telescopes*, *New Journal of Physics* **11** (2009) 065011.

[18] Y. Itikawa, M. Hayashi, A. Ichimura, K. Onda, K. Sakimoto, K. Takayanagi et al., *Cross sections for collisions of electrons and photons with nitrogen molecules*, *Journal of Physical and Chemical Reference Data* **15** (1986) 985 [https://doi.org/10.1063/1.555762].

[19] M. Ave, M. Bohacova, B. Buonomo, N. Busca, L. Cazon, S. Chemerisov et al., *Measurement of the pressure dependence of air fluorescence emission induced by electrons*, *Astroparticle Physics* **28** (2007) 41.

[20] M. Ave, M. Bohacova, B. Buonomo, N. Busca, L. Cazon, S. Chemerisov et al., *Temperature and humidity dependence of air fluorescence yield measured by AIRFLY*, *Nuclear Instruments and Methods in Physics Research Section A: Accelerators, Spectrometers, Detectors and Associated Equipment* **597** (2008) 50.

[21] J. Bolmont, P. Corona, P. Gauron, P. Ghislain, C. Goffin, L.G. Riveros et al., *The camera of the fifth h.e.s.s. telescope. part i: System description*, *Nuclear Instruments and Methods in Physics Research Section A: Accelerators, Spectrometers, Detectors and Associated Equipment* **761** (2014) 46.

[22] K. Bernlöhr, *Simulation of imaging atmospheric cherenkov telescopes with CORSIKA and sim_telarray*, *Astroparticle Physics* **30** (2008) 149.

[23] D. Heck, J. Knapp, J.N. Capdevielle, G. Schatz and T. Thouw, *Corsika: A monte carlo code to simulate extensive air showers*, Tech. Rep. (1998), DOI.

[24] H.E. Dixon, J.C. Earnshaw, J.R. Hook, J.H. Hough, G.J. Smith, W. Stephenson et al., *Computer Simulations of Cosmic-Ray Air Showers. I. Average Characteristics of Proton Initiated Showers*, *Proceedings of the Royal Society of London Series A* **339** (1974) 133.

[25] T. Pierog, I. Karpenko, J.M. Katzy, E. Yatsenko and K. Werner, *Epos lhc: Test of collective hadronization with data measured at the cern large hadron collider*, *Phys. Rev. C* **92** (2015) 034906.

[26] W.R. Nelson, H. Hirayama and D.W. Rogers, *Egs4 code system*, .

[27] N. Kalmykov, S. Ostapchenko and A. Pavlov, *Quark-gluon-string model and eas simulation problems at ultra-high energies*, *Nuclear Physics B - Proceedings Supplements* **52** (1997) 17.

[28] H. Fesefeldt, *The simulation of hadronic shower - physics and applications, pitha-85/02, rwth aachen*, 1985.